CEERS Key Paper. II. A First Look at the Resolved Host Properties of AGN at $3 < z < 5$ with JWST

Dale D. Kocevski, Guillermo Barro, Elizabeth J. Mcgrath, Steven L. Finkelstein, Micaela B. Bagley, Henry C. Ferguson, Shardha Jogee, Guang Yang, Mark Dickinson, Nimish P. Hathi, et al.

The Astrophysical Journal Letters, 946:L14 (14pp), 2023 March 20 https://doi.org/10.3847/2041-8213/acad00

CEERS Key Paper. II. A First Look at the Resolved Host Properties of AGN at $3 < z < 5$ with JWST

Dale D. Kocevski[1], Guillermo Barro[2], Elizabeth J. McGrath[1], Steven L. Finkelstein[3], Micaela B. Bagley[3], Henry C. Ferguson[4], Shardha Jogee[3], Guang Yang[5,6], Mark Dickinson[7], Nimish P. Hathi[4], Bren E. Backhaus[8], Eric F. Bell[9], Laura Bisigello[10,11], Véronique Buat[12], Denis Burgarella[12], Caitlin M. Casey[3], Nikko J. Cleri[13,14], M. C. Cooper[15], Luca Costantin[16], Darren Croton[17,18], Emanuele Daddi[19], Adriano Fontana[20], Seiji Fujimoto[21,22,23,52], Jonathan P. Gardner[24], Eric Gawiser[25], Mauro Giavalisco[26], Andrea Grazian[11], Norman A. Grogin[4], Yuchen Guo[3], Pablo Arrabal Haro[7], Michaela Hirschmann[27], Benne W. Holwerda[28], Marc Huertas-Company[29,30,31], Taylor A. Hutchison[13,14,32,53,54], Kartheik G. Iyer[33], Brenda Jones[34], Stéphanie Juneau[35], Jeyhan S. Kartaltepe[36], Lisa J. Kewley[37], Allison Kirkpatrick[38], Anton M. Koekemoer[39], Peter Kurczynski[40], Aurélien Le Bail[19], Arianna S. Long[21,52], Jennifer M. Lotz[41], Ray A. Lucas[39], Casey Papovich[13,14], Laura Pentericci[20], Pablo G. Pérez-González[42], Nor Pirzkal[43], Marc Rafelski[39,44], Swara Ravindranath[39], Rachel S. Somerville[45], Amber N. Straughn[32], Sandro Tacchella[46,47], Jonathan R. Trump[8], Stephen M. Wilkins[48,49], Stijn Wuyts[50], L. Y. Aaron Yung[32,54], and Jorge A. Zavala[51]

[1] Department of Physics and Astronomy, Colby College, Waterville, ME 04901, USA; dale.kocevski@colby.edu
[2] Department of Physics, University of the Pacific, Stockton, CA 90340, USA
[3] Department of Astronomy, The University of Texas at Austin, Austin, TX, USA
[4] Space Telescope Science Institute, Baltimore, MD, USA
[5] Kapteyn Astronomical Institute, University of Groningen, P.O. Box 800, 9700 AV Groningen, The Netherlands
[6] SRON Netherlands Institute for Space Research, Postbus 800, 9700 AV Groningen, The Netherlands
[7] NSF's National Optical-Infrared Astronomy Research Laboratory, 950 North Cherry Avenue, Tucson, AZ 85719, USA
[8] Department of Physics, University of Connecticut, 196 Auditorium Road, Unit 3046, Storrs, CT 06269, USA
[9] Department of Astronomy, University of Michigan, 1085 South University Avenue, Ann Arbor, MI 48109-1107, USA
[10] Dipartimento di Fisica e Astronomia "G.Galilei," Universitá di Padova, Via Marzolo 8, I-35131 Padova, Italy
[11] INAF–Osservatorio Astronomico di Padova, Vicolo dell'Osservatorio 5, I-35122, Padova, Italy
[12] Aix Marseille Univ, CNRS, CNES, LAM Marseille, France
[13] Department of Physics and Astronomy, Texas A&M University, College Station, TX 77843-4242, USA
[14] George P. and Cynthia Woods Mitchell Institute for Fundamental Physics and Astronomy, Texas A&M University, College Station, TX 77843-4242, USA
[15] Department of Physics & Astronomy, University of California, Irvine, 4129 Reines Hall, Irvine, CA 92697, USA
[16] Centro de Astrobiología (CSIC-INTA), Ctra de Ajalvir km 4, Torrejón de Ardoz, E-28850, Madrid, Spain
[17] Centre for Astrophysics & Supercomputing, Swinburne University of Technology, Hawthorn, VIC 3122, Australia
[18] ARC Centre of Excellence for All Sky Astrophysics in 3 Dimensions (ASTRO 3D), Australia
[19] Université Paris-Saclay, Université Paris Cité, CEA, CNRS, AIM, F-91191, Gif-sur-Yvette, France
[20] INAF–Osservatorio Astronomico di Roma, via di Frascati 33, I-00078 Monte Porzio Catone, Italy
[21] Department of Astronomy, The University of Texas at Austin, Austin, TX 78712, USA
[22] Cosmic Dawn Center (DAWN), Jagtvej 128, DK-2200 Copenhagen N, Denmark
[23] Niels Bohr Institute, University of Copenhagen, Lyngbyvej 2, DK-2100 Copenhagen Ø, Denmark
[24] Astrophysics Science Division, Goddard Space Flight Center, Code 665, Greenbelt, MD 20771, USA
[25] Department of Physics and Astronomy, Rutgers, the State University of New Jersey, Piscataway, NJ 08854, USA
[26] University of Massachusetts Amherst, 710 North Pleasant Street, Amherst, MA 01003-9305, USA
[27] Institute of Physics, Laboratory of Galaxy Evolution, Ecole Polytechnique Fédérale de Lausanne (EPFL), Observatoire de Sauverny, 1290 Versoix, Switzerland
[28] Physics & Astronomy Department, University of Louisville, Louisville, KY 40292, USA
[29] Instituto de Astrofísica de Canarias, La Laguna, Tenerife, Spain
[30] Universidad de la Laguna, La Laguna, Tenerife, Spain
[31] Université Paris-Cité, LERMA—Observatoire de Paris, PSL, Paris, France
[32] Astrophysics Science Division, NASA Goddard Space Flight Center, 8800 Greenbelt Road, Greenbelt, MD 20771, USA
[33] Dunlap Institute for Astronomy & Astrophysics, University of Toronto, Toronto, ON M5S 3H4, Canada
[34] Department of Physics and Astronomy, University of Maine, Orono, ME 04469-5709, USA
[35] NSF's NOIRLab, 950 North Cherry Avenue, Tucson, AZ 85719, USA
[36] Laboratory for Multiwavelength Astrophysics, School of Physics and Astronomy, Rochester Institute of Technology, 84 Lomb Memorial Drive, Rochester, NY 14623, USA
[37] Center for Astrophysics | Harvard & Smithsonian, 60 Garden Street, Cambridge, MA 02138, USA
[38] Department of Physics and Astronomy, University of Kansas, Lawrence, KS 66045, USA
[39] Space Telescope Science Institute, 3700 San Martin Drive, Baltimore, MD 21218, USA
[40] Observational Cosmology Laboratory (Code 665), NASA Goddard Space Flight Center, Greenbelt, MD 20771, USA
[41] Gemini Observatory/NSF's National Optical-Infrared Astronomy Research Laboratory, 950 North Cherry Avenue, Tucson, AZ 85719, USA
[42] Centro de Astrobiología (CAB), CSIC-INTA, Ctra. de Ajalvir km 4, Torrejón de Ardoz, E-28850, Madrid, Spain
[43] ESA/AURA Space Telescope Science Institute, USA
[44] Department of Physics and Astronomy, Johns Hopkins University, Baltimore, MD 21218, USA
[45] Center for Computational Astrophysics, Flatiron Institute, 162 5th Avenue, New York, NY 10010, USA
[46] Kavli Institute for Cosmology, University of Cambridge, Madingley Road, Cambridge, CB3 0HA, UK
[47] Cavendish Laboratory, University of Cambridge, 19 JJ Thomson Avenue, Cambridge, CB3 0HE, UK
[48] Astronomy Centre, University of Sussex, Falmer, Brighton BN1 9QH, UK
[49] Institute of Space Sciences and Astronomy, University of Malta, Msida MSD 2080, Malta
[50] Department of Physics, University of Bath, Claverton Down, Bath BA2 7AY, UK

[51] National Astronomical Observatory of Japan, 2-21-1 Osawa, Mitaka, Tokyo 181-8588, Japan
Received 2022 September 2; revised 2022 November 21; accepted 2022 November 21; published 2023 March 27

Abstract

We report on the host properties of five X-ray-luminous active galactic nuclei (AGN) identified at $3 < z < 5$ in the first epoch of imaging from the Cosmic Evolution Early Release Science Survey. Each galaxy has been imaged with the JWST Near-Infrared Camera, which provides rest-frame optical morphologies at these redshifts. We also derive stellar masses and star formation rates for each host by fitting its spectral energy distribution using a combination of galaxy and AGN templates. We find that three of the AGN hosts have spheroidal morphologies, one is a bulge-dominated disk, and one is dominated by pointlike emission. None are found to show strong morphological disturbances that might indicate a recent interaction or merger event. When compared to a sample of mass-matched inactive galaxies, we find that the AGN hosts have morphologies that are less disturbed and more bulge-dominated. Notably, all four of the resolved hosts have rest-frame optical colors consistent with a quenched or poststarburst stellar population. The presence of AGN in passively evolving galaxies at $z > 3$ is significant because a rapid feedback mechanism is required in most semianalytic models and cosmological simulations to explain the growing population of massive quiescent galaxies observed at these redshifts. Our findings show that AGN can continue to inject energy into these systems after their star formation is curtailed, potentially heating their halos and preventing renewed star formation. Additional observations will be needed to determine what role this feedback may play in helping to quench these systems and/or maintain their quiescent state.

Unified Astronomy Thesaurus concepts: AGN host galaxies (2017); Supermassive black holes (1663)

1. Introduction

The role that supermassive black holes (SMBHs) play in the evolution of galaxies remains a heavily debated topic within extragalactic astronomy. There are signs that the growth of SMBHs and their host galaxies is closely connected, as evidenced by a variety of tight scaling relationships (e.g., Magorrian et al. 1998; Ferrarese & Merritt 2000; Gebhardt et al. 2000; McConnell & Ma 2013; Sun et al. 2015) and the need for energy injection in massive galaxies to limit their star formation activity (Benson et al. 2003; Croton et al. 2006; Somerville et al. 2008). As a result, active galactic nuclei (AGN) have become key components in many galaxy evolution models (e.g., Hirschmann et al. 2012; Dubois et al. 2016; Weinberger et al. 2018; Dave et al. 2019; Chen et al. 2020; Yung et al. 2021). However, several open issues remain in our understanding of how the SMBH–galaxy connection is established and maintained. Among these are the mechanism(s) responsible for fueling the bulk of SMBH growth across cosmic time and the role of AGN in quenching the first generation of massive, quiescent galaxies.

The study of AGN host morphologies has been widely used to place constraints on the first of these issues. Galaxy mergers are often invoked as a key process to potentially drive the coevolution of galaxies and SMBHs due to their effectiveness at dissipating angular momentum and driving gas inflows that can both fuel black hole growth and build the stellar bulge via centrally concentrated starbursts (e.g., Sanders et al. 1988; Kauffmann & Haehnelt 2000; Di Matteo et al. 2005; Springel et al. 2005b; Jogee 2006; Hopkins et al. 2008b). However, studies of X-ray-selected AGN out to $z \sim 2$ find that their host morphologies are no more disturbed than those of similar inactive galaxies (Grogin et al. 2005; Pierce et al. 2007; Cisternas et al. 2011; Schawinski et al. 2011; Kocevski et al. 2012; Villforth et al. 2014; Rosario et al. 2015). This suggests that other mechanisms, such as minor mergers, Toomre-unstable clumpy disks, or secular angular momentum loss, play a larger role in fueling moderate-luminosity AGN at these redshifts than previously thought (Hopkins et al. 2014).

A major caveat to these results is that SMBHs are predicted to accrete the bulk of their mass while heavily obscured and hydrodynamical simulations predict that this obscured phase should coincide with the most morphologically disturbed period of a galaxy interaction (Hopkins et al. 2006). The morphologies of infrared-selected AGN and Compton-thick X-ray AGN do indeed show increased signs of disturbance relative to their unobscured counterparts, in apparent agreement with this scenario (Koss et al. 2010; Satyapal et al. 2014; Kocevski et al. 2015; Donley et al. 2018). At higher redshifts ($z > 3$), however, the rest-frame optical morphologies of AGN have remained relatively unconstrained due to the fact that the reddest Hubble Space Telescope (HST) band, F160W, probes blueward of the Balmer break at these redshifts.

Another open question is whether AGN drive the quenching of star formation in massive galaxies. Most cosmological models and simulations require a feedback mechanism to reproduce the properties of the massive galaxy population (Springel et al. 2005a; Croton et al. 2006; Somerville et al. 2008; Choi et al. 2015; Weinberger et al. 2018; Dave et al. 2019), the needed energetics of which are not easily achieved by stellar feedback alone (e.g., Bower et al. 2006). While AGN feedback has been implemented in a variety of ways (see Somerville & Dave 2015 for a review), a common prescription in semianalytic models involves major mergers that trigger AGN-driven winds that expel gas and eventually truncate the galaxy's star formation activity (Hopkins et al. 2008a, 2008b).

Although widely adopted, observational evidence for this scenario has remained elusive. Demographic studies have produced mixed results, with findings of both negative and positive correlations between AGN activity and host properties such as star formation rates (SFRs), rest-frame colors, and molecular gas content (Nandra et al. 2007; Schawinski et al.

[52] Hubble Fellow.
[53] NSF Graduate Fellow.
[54] NASA Postdoctoral Fellow.

2007; Harrison et al. 2012; Mullaney et al. 2012; Stanley et al. 2015; Kirkpatrick et al. 2019; Stacey et al. 2021; Mountrichas et al. 2022). However, there is a general consensus that X-ray-selected AGN at $z \sim 2$ are preferentially located in gas-rich, heavily star-forming galaxies (e.g., Rosario et al. 2015; Florez et al. 2020, 2021; Mountrichas et al. 2021; Ji et al. 2022). The few studies that have probed beyond $z \sim 3$ using HST have also found that AGN are more likely to be hosted by star-forming systems (Aird et al. 2018; Suh et al. 2019). Ward et al. (2022) pointed out that this is not necessarily in tension with the AGN feedback scenario given the common fuel supply that drives both AGN and star formation and the potential time delay between AGN activity and its effects.

At higher redshifts ($z = 3$–5), the discovery of a growing population of massive ($M_* > 10^{11}\ M_\odot$) galaxies that fully quenched 1–2 Gyr after the Big Bang further necessitates a rapid and efficient quenching mechanism (Schreiber et al. 2018; Forrest et al. 2020a, 2020b; Carnall et al. 2022; Labbe et al. 2022). However, the role that AGN play in this process is still uncertain, with some models finding that AGN feedback is not the leading mechanism shaping the bright end of the galaxy luminosity function at these redshifts (Yung et al. 2019a, 2019b). If AGN are the drivers of early quenching among massive galaxies, we may see signatures of their impact on the properties of their host galaxies during this epoch.

In this study, we provide a first look at the rest-frame optical morphology and star formation activity of galaxies hosting X-ray-selected AGN at $3 < z < 5$ using NIRCam imaging from the James Webb Space Telescope (JWST; Gardner et al. 2006). Our analysis is presented as follows. In Section 2, we describe the near-infrared imaging and X-ray data used for this study, while Section 3 describes our methodology for identifying AGN at our target redshift range. Section 4 describes our results, and the implications of our findings are discussed in Section 5. When necessary, the following cosmological parameters are used: $H_0 = 70\ \mathrm{km\ s^{-1}\ Mpc^{-1}}$ and $\Omega_{\rm tot}$, Ω_Λ, $\Omega_m = 1$, 0.7, 0.3.

2. Observations and Data Description

2.1. CEERS Data

The Cosmic Evolution Early Release Science Survey (CEERS) is an early release science program that will cover 100 arcmin^2 of the Extended Groth Strip (EGS) with imaging and spectroscopy using coordinated, overlapping parallel observations by most of the JWST instrument suite. CEERS is based around a mosaic of 10 NIRCam pointings, with six NIRSpec and six MIRI pointings observed in parallel. Here we make use of the first four CEERS NIRCam pointings (hereafter epoch 1), obtained on 2022 June 21, known as CEERS1, CEERS2, CEERS3, and CEERS6. In each NIRCam pointing, data were obtained in the short-wavelength (SW) channel F115W, F150W, and F200W filters and long-wavelength (LW) channel F277W, F356W, F410M, and F444W filters. The total exposure time for the pixels observed in all three dithers was typically 2835 s filter^{-1}.

We performed an initial reduction of the NIRCam images in all four pointings using version 1.5.3 of the JWST Calibration Pipeline[55] with some custom modifications. We used the current (2022 July 15) set of NIRCam reference files,[56] though we note that the majority were created preflight, including the flats and photometric calibration references. We describe our reduction steps in greater detail in Finkelstein et al. (2022) and M. B. Bagley et al. 2022, (in preparation). Coadding the reduced observations into a single mosaic was performed using the drizzle algorithm with an inverse variance map weighting (Casertano et al. 2000; Fruchter & Hook 2002) via the Resample step in the pipeline. The output mosaics have pixel scales of $0\farcs03$ pixel^{-1}.

Photometry was computed on point-spread function (PSF)–matched images using SExtractor (Bertin & Arnouts 1996) v2.25.0 in two-image mode, with an inverse variance weighted combination of the PSF-matched F277W and F356W images as the detection image. Photometry was measured in all seven of the NIRCam bands observed by CEERS, as well as the F606W, F814W, F105W, F125W, F140W, and F160W HST bands using data obtained by the CANDELS and 3D-HST surveys (Grogin et al. 2011; Koekemoer et al. 2011; Brammer et al. 2012).

2.2. X-Ray Observations

The X-ray data used for this study come from the AEGIS-XD survey (Nandra et al. 2015; hereafter N15), which consists of Chandra ACIS-I observations with a characteristic exposure time of 800 ks over all four of the epoch 1 CEERS pointings. The survey has a flux limit of 1.5×10^{-16} erg cm^{-2} s^{-1} in the 0.5–10 keV band, which corresponds to a luminosity limit that ranges from 5.3×10^{42} erg s^{-1} at $z = 3$ to 1.7×10^{43} erg s^{-1} at $z = 5$.

We make use of the published X-ray point-source catalog and counterpart associations presented in N15. These associations were made by matching to a Spitzer/IRAC 3.6 μm selected photometric catalog provided by the Rainbow Cosmological Surveys Database (Barro et al. 2011a, 2011b). To take advantage of the increased spatial resolution provided by NIRCam, we independently cross-match the X-ray source list to our F277W+F356W-selected catalog using the maximum-likelihood technique described by Sutherland & Saunders (1992). We find 48 X-ray sources matched to F277W +F356W counterparts in the CEERS imaging.

3. Sample Selection

We use the EAzY (Brammer et al. 2008) software to estimate the photometric redshifts of all sources in our multiwavelength photometric catalog. The spectral energy distribution (SED) fits were carried out using photometry in all seven of the NIRCam bands and all six of the HST bands in our catalog. The redshift range was allowed to vary from zero to 12, and we used no zero-point corrections or luminosity priors. We chose the default template set *tweak_fsps_QSF_12_v3*, which was generated using the flexible stellar population synthesis code (Conroy et al. 2009; Conroy & Gunn 2010).

Using a combination of our photometric redshifts and a compilation of published spectroscopic redshifts in the EGS field (N. Hathi 2022, private communication), we identify five X-ray-detected AGN that have redshifts of $z > 3$ in the current epoch of CEERS imaging. These five AGN comprise our primary sample and are the focus of this study. One of these sources, AEGIS 482, has a spectroscopic redshift of $z = 3.465$ from the DEEP2 survey (Newman et al. 2013), while the remainder have photometric redshifts. Information about each AGN in our sample is listed in Table 1.

The X-ray luminosity versus redshift distribution of our $z > 3$ sample is shown in Figure 1, along with the X-ray

[55] jwst-pipeline.readthedocs.io/en/latest/
[56] jwst-crds.stsci.edu, jwst_nircam_0214.imap.

Table 1
Properties of Our Primary Sample of X-Ray-Detected AGN at $3 < z < 5$

AEGIS-XD ID	R.A. (J2000)	Decl. (J2000)	z	log $(M_*/M_\odot)$	$L_{X,2-10\ keV}$ ($\times 10^{43}$ erg s^{-1})	SFR ($M_\odot$ yr^{-1})	A_v	n	$V-J$	$U-V$
AEGIS 482	214.755245	52.836807	3.465	$9.79^{+0.08}_{-0.04}$	$11.38^{+0.98}_{-0.91}$	$24.0^{+16.8}_{-14.9}$	$0.1^{+0.3}_{-0.1}$	...	0.16	0.29
AEGIS 495	214.871261	52.845092	$3.54^{+0.05}_{-0.03}$	$11.01^{+0.10}_{-0.02}$	$0.78^{+0.41}_{-0.31}$	$52.5^{+29.3}_{-32.5}$	$1.0^{+0.8}_{-0.6}$	2.24 ± 0.02	0.88	1.35
AEGIS 511	214.895659	52.856515	$3.21^{+0.01}_{-0.01}$	$10.90^{+0.08}_{-0.04}$	$2.22^{+0.55}_{-0.47}$	$3.6^{+5.1}_{-1.6}$	$0.2^{+0.3}_{-0.2}$	3.49 ± 0.01	0.53	1.50
AEGIS 525	214.853928	52.861366	$3.54^{+0.03}_{-0.10}$	$11.37^{+0.04}_{-0.04}$	$2.58^{+0.60}_{-0.51}$	$10.7^{+1.0}_{-9.1}$	$1.9^{+0.1}_{-0.4}$	4.20 ± 0.04	1.57	2.14
AEGIS 532	214.850584	52.866030	$4.10^{+0.05}_{-0.05}$	$10.82^{+0.06}_{-0.03}$	$2.92^{+0.80}_{-0.67}$	$0.5^{+0.1}_{-0.1}$	$0.4^{+0.4}_{-0.4}$	1.14 ± 0.05	0.97	1.63

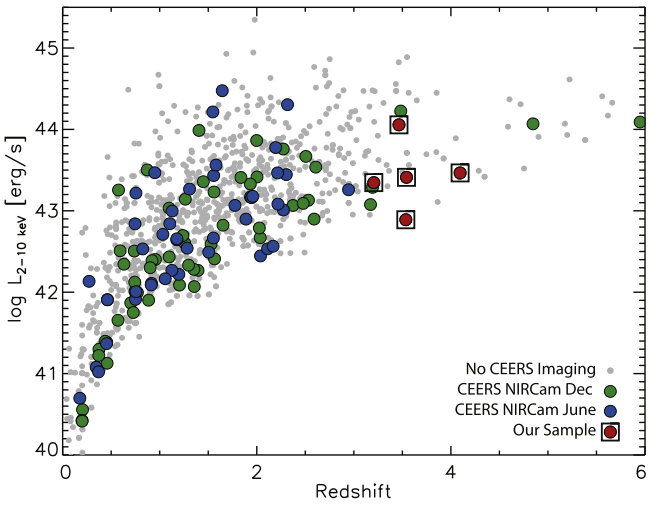

Figure 1. The X-ray luminosity in the rest-frame 2–10 keV band as a function of redshift for the AEGIS-XD sample. The 2–10 keV luminosity is derived from the 0.5–10 keV flux, *k*-corrected using a power-law X-ray spectrum with a spectral index of $\Gamma = 1.4$. Sources that fall within the first epoch of CEERS imaging are shown in blue, while those that we anticipate observing in the next epoch of CEERS imaging are shown in green. The five X-ray AGN observed by CEERS at $3 < z < 5$ are shown as boxed red circles.

luminosities of the entire AEGIS-XD sample, including sources that we anticipate will be observed with NIRCam in the next epoch of CEERS imaging. Our primary sample has rest-frame 2–10 keV X-ray luminosities ranging from 7.76×10^{42} to 1.14×10^{44} erg s^{-1} (see Table 1), with an average luminosity of 3.98×10^{43} erg s^{-1}. Hardness ratios (HRs) reported in N15 measured using the counts in the 0.5–2 and 2–7 keV bands show that AEGIS 482, AEGIS 495, and AEGIS 511 all have relatively unabsorbed emission (HR < 0), while AEGIS 525 and AEGIS 532 have harder emission indicative of a higher obscuring column density.

All but one X-ray source, AEGIS 532, have counterparts that agree with those published in N15. AEGIS 532, however, was previously associated with a large foreground disk at $z = 2.14$, but the X-ray emission is better centered on a neighboring galaxy that we estimate to be at $z = 4.1$. This can be seen in Figure 2, which shows the contours of the adaptively smoothed X-ray emission of each source overlaid on NIRCam imaging in the F356W band. This source was not previously detected by the CANDELS survey and is blended with the foreground galaxy in the 3.6 μm Spitzer IRAC imaging used for counterpart matching by N15.

We note that although the photometric redshifts from EAzY are calculated without accounting for AGN emission, we find only a moderate AGN contribution to the galaxy SEDs of most of our sample (see Section 5). The only exception is AEGIS 482, but this source has a spectroscopically determined redshift. Nonetheless, we checked the EAzY-derived redshifts of the five galaxies in our sample against those obtained from the X-CIGALE software (Yang et al. 2020), which performs SED fits using both AGN and stellar templates. With the exception of AEGIS 482, which is our most X-ray-luminous source, we find a good general agreement between the two sets of redshifts.

4. Methodology

Images of our AGN sample in five NIRCam bands can be seen in Figure 3. We assessed the morphology of their host galaxies through a combination of visual inspection, nonparametric morphology indicators, and surface brightness profile fitting. The visual classifications were carried out using the classification scheme presented in Kocevski et al. (2015). The surface brightness profile modeling was performed with the GALFIT software (Peng et al. 2002) in the F356W band, which probes light redward of the Balmer break at the redshifts of all galaxies in the sample. We provide GALFIT with empirical PSFs constructed from the four CEERS pointings and noise images that account for both the intrinsic image noise (e.g., background and readout noise) and added Poisson noise due to the objects themselves. We fit each galaxy with a single Sérsic profile (Sérsic 1968) but explore the need for additional components to help minimize the flux in our residual images. Neighboring objects were fit simultaneously using single Sérsic models.

The nonparametric morphologies were measured using the Python package Statmorph[57] (Rodriguez-Gomez et al. 2019) in the F356W band. For our analysis, we make use of the following morphology statistics: the Gini coefficient (G; Abraham et al. 2003; Lotz et al. 2004), the second moment of the region of the galaxy containing 20% of the total flux (M_{20}; Lotz et al. 2004), the Gini–M_{20} bulge statistic ($F(G, M_{20})$; Snyder et al. 2015), concentration (C; Bershady et al. 2000; Conselice 2003), and asymmetry (A; Conselice et al. 2000).

Stellar masses (M_*) and SFRs were determined by performing SED fits using FAST v1.1 (Kriek et al. 2009; Aird et al. 2018), which allows for simultaneous fitting of both galaxy and AGN components. For these fits, we assume a Chabrier (2003) initial mass function, Bruzual & Charlot (2003) stellar population models, fixed solar metallicity, dust reddening of A_V in the range 0–4 mag (assuming the Kriek & Conroy 2013 dust attenuation curves), and "delayed-τ" star formation histories, with τ in the range 0.1–10 Gyr (e.g., Maraston et al. 2010). We allow for an AGN component in the SED fit, adopting a library of eight empirically determined AGN templates. These include five AGN-dominated templates from the Polletta et al. (2007) SWIRE template library (namely, the Torus, TQSO1, BQSO1, QSO1, and QSO2 templates) and

[57] https://statmorph.readthedocs.io/en/latest/

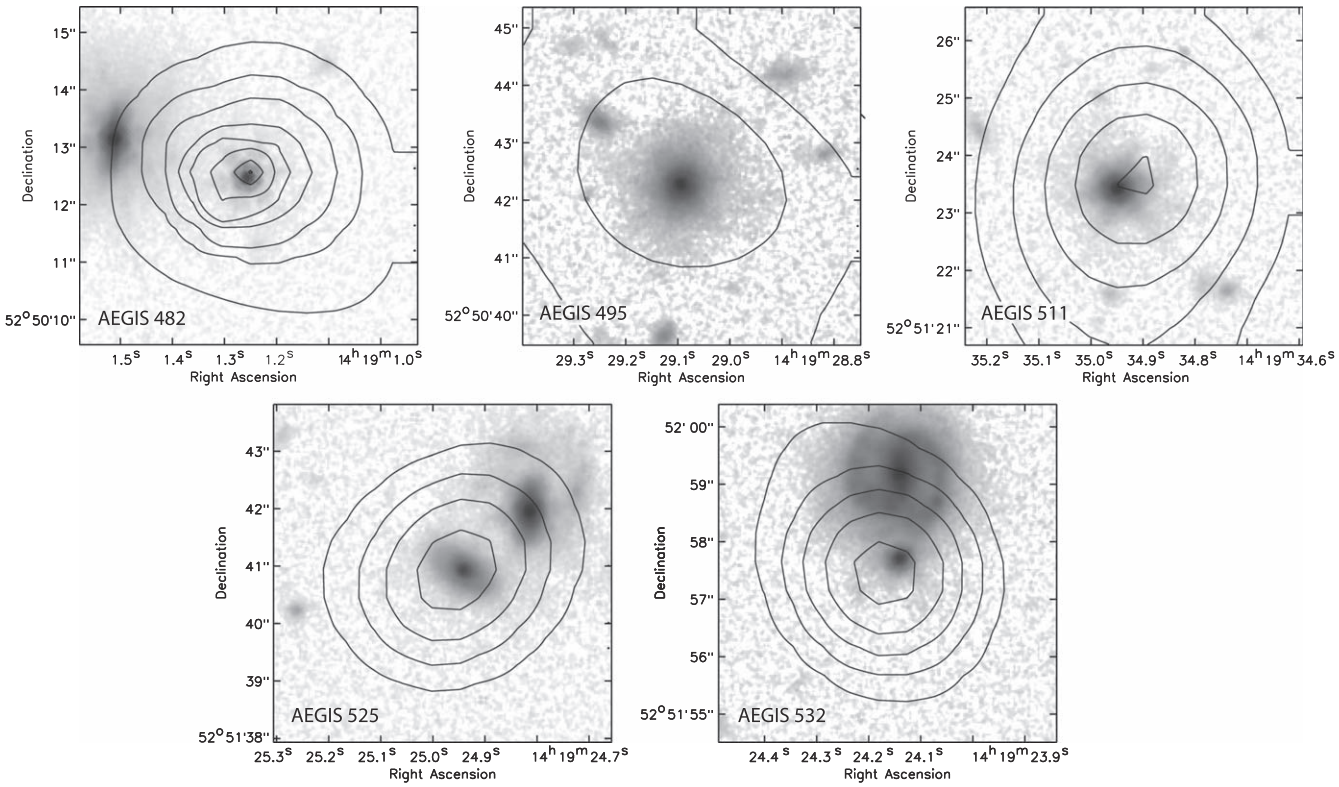

Figure 2. The X-ray emission contours overlaid on F356W images of the five AGN host galaxies with $3 < z < 5$ found in the first epoch of CEERS imaging. The X-ray emission is adaptively smoothed using the asmooth algorithm (Ebeling et al. 2006). The contour levels begin at 1.5 times the local background and are logarithmically spaced thereafter.

three composite SEDs of X-ray-selected AGN with absorption column densities of $N_{\rm H} = 10^{22-23}$, 10^{23-24}, and 10^{24-25} cm^{-2} from Silva et al. (2004). See Appendix A of Aird et al. (2018) for additional details. Our two-component SED fits provide a measure of various host properties (i.e., stellar mass, SFR, and rest-frame colors) corrected for any contamination from nonstellar nuclear light. Photometry in all of the JWST and HST bands discussed in Section 2.1 was used for these fits.

We note that as an additional test, we also performed SED fitting with X-CIGALE and found very good agreement between our derived host properties. We find the average difference between our derived masses to be 0.2 dex. Our *UVJ* colors are also consistent, with no change to the star-forming/quiescent classification of any AGN host. None of our primary conclusions would change if we employed one SED fitting code instead of the other.

4.1. Inactive Control Sample

In order to compare the morphologies of our AGN sample to similar inactive galaxies (i.e., those with no X-ray detection), we construct a control sample of galaxies with similar redshifts and masses to those of the well-resolved AGN hosts at $z > 3$. For each AGN except AEGIS 482, we selected four X-ray-undetected galaxies with masses greater than $\log(M_*/M_\odot) = 10.5$ and redshifts in the range $3.0 < z < 4.5$. The resulting sample of 16 galaxies has an average stellar mass of $\log(M_*/M_\odot) = 10.87$, compared to the 11.0 average for the well-resolved AGN hosts (see Section 5). The redshift versus stellar mass of the control sample in comparison to our primary AGN sample is shown in Figure 4, while multiwavelength image cutouts of the control galaxies are presented in Figure 5. We assess the morphology of these galaxies using identical visual classifications, nonparametric statistics, and GALFIT modeling, as is carried out on the AGN sample.

5. Host Galaxy Properties

The results of our two-component SED fits can be seen in Figure 6. We find that three of the five sources (AEGIS 495, AEGIS 525, and AEGIS 532) are fit with a moderate (<10%) AGN contribution to the flux in the F356W band. The nonstellar contribution rises to 31% in AEGIS 511 and accounts for 70% of the flux from AEGIS 482, whose SED is best fit using a type 1 QSO template. The former shows signs of diffraction spikes in our LW images, consistent with a nuclear point source, while the latter is dominated by pointlike emission in both the JWST and HST imaging (see Section 4.1 below). Furthermore, the spectrum of AEGIS 482 from the DEEP2 survey shows broad C III and C IV emission lines, consistent with the QSO SED fit to this source.

We find that the four well-resolved hosts have stellar masses in the range of $\log(M_*/M_\odot) = 10.82 - 11.37$ (see Table 1), making them among the most massive galaxies detected at this redshift range in the current CEERS pointings (S. L. Finkelstein et al. 2022, in preparation), even after accounting for nuclear light from the AGN. Our best-fit mass for AEGIS 482 is $\log(M_*/M_\odot) = 9.79$, which appears inconsistent with the $M_*-L_{\rm X}$ relationship reported by Suh et al. (2019) and may imply that too much light has been attributed to the AGN in our two-component SED fit. That said, an independent analysis of this source by Ding et al. (2022) using the gsf software (Morishita et al. 2019) finds a mass of 9.55, in general agreement with our measurement.

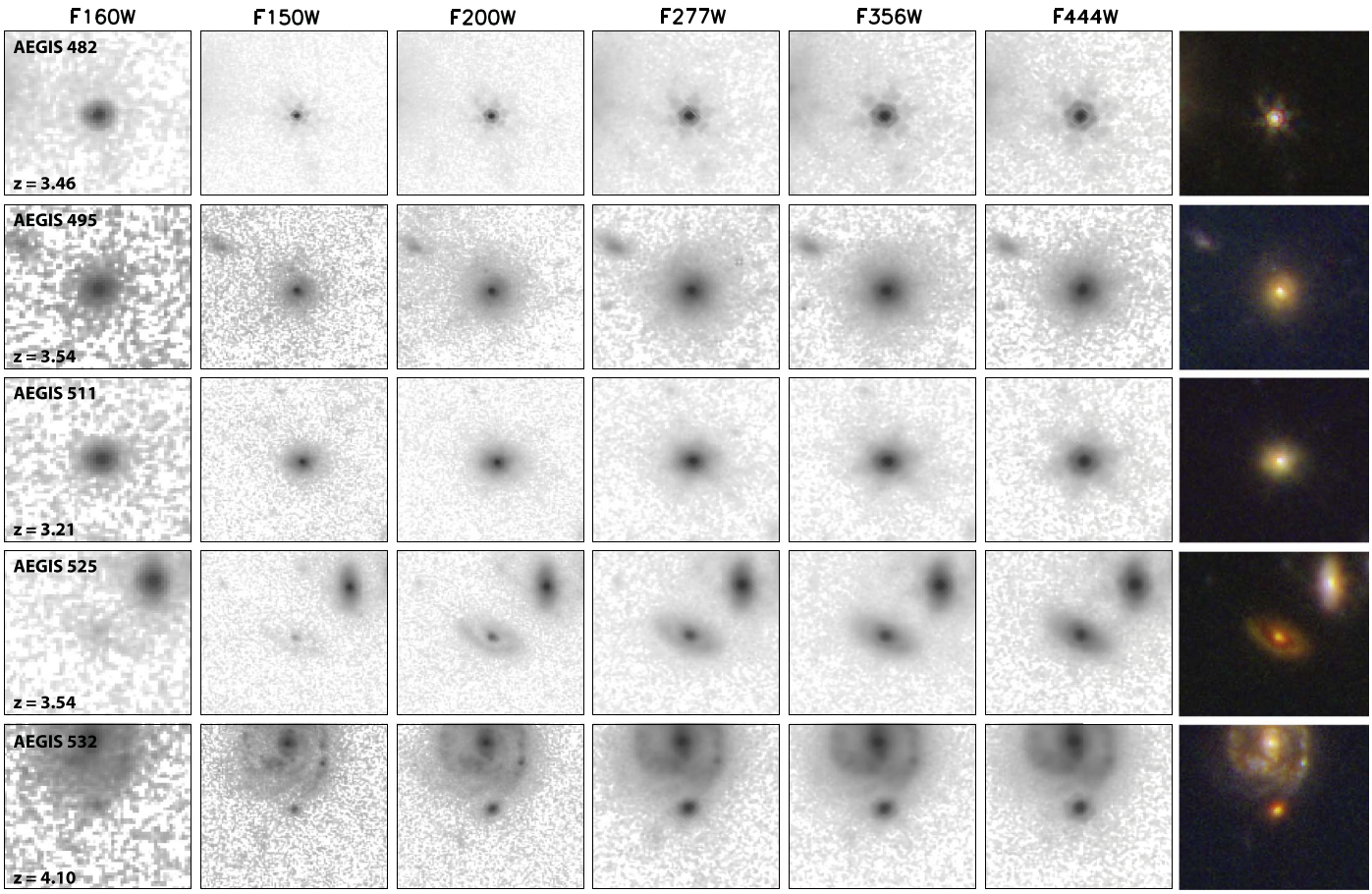

Figure 3. Multiwavelength image cutouts of our primary AGN sample at $z > 3$. The images shown were taken in the F160W HST WFC3 filter and five JWST NIRCam SW (F150W and F200W) and LW (F277W, F356W, and F444W) filters. The RGB images are composed of images in the F150W, F200W, and F277W filters. All images are $3\farcs5 \times 3\farcs5$ in size.

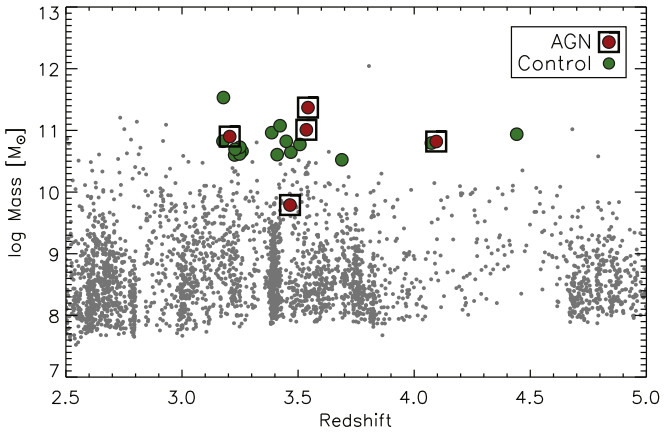

Figure 4. Stellar mass vs. redshift for galaxies in the first epoch of CEERS NIRCam imaging. Our primary sample of AGN hosts at $z > 3$ is shown as boxed red circles, while our control sample of inactive galaxies is shown as green circles. See Section 4.1 for details.

In the following sections, we examine the morphologies and star formation activity of these galaxies in greater detail.

5.1. Morphologies

5.1.1. Visual Classifications

Based on our visual classifications, three of the AGN (AEGIS 495, AEGIS 511, and AEGIS 532) have spheroidal hosts, while one (AEGIS 525) is found in a disk galaxy with a prominent bulge component at longer wavelengths. The final source (AEGIS 482) appears pointlike in all seven NIRCam filters observed by CEERS. Our SED fit for AEGIS 525, the single disk in the sample, finds that minimal AGN light is needed in the reddest NIRCam bandpasses, suggesting that the central bulge component is indeed a stellar bulge and not nuclear emission from the AGN. Finally, none of the AGN hosts show strong asymmetries or distortions that might indicate a recent interaction or merger event. All of them are visually classified as undisturbed. The close companions to AEGIS 525 and AEGIS 532 are both foreground galaxies seen in projection, with redshifts of 1.35 and 2.07, respectively.

The inactive control sample, in comparison, exhibits a wider distribution of morphologies. Based on visual inspection, 50% (8/16) have disk-dominated morphologies, 37.5% (6/16) are bulge-dominated, and 12.5% (2/16) are classified as irregular. Furthermore, 50% (8/16) of the sample shows some level of asymmetry or distortion that might be indicative of a recent interaction, while 25% (4/16) are distorted enough to be classified as ongoing mergers. In summary, the control sample appears diskier and more disturbed than the AGN host galaxies. However, we caution that a larger sample of massive galaxies (both active and inactive) will be needed to determine if these differences are statistically significant.

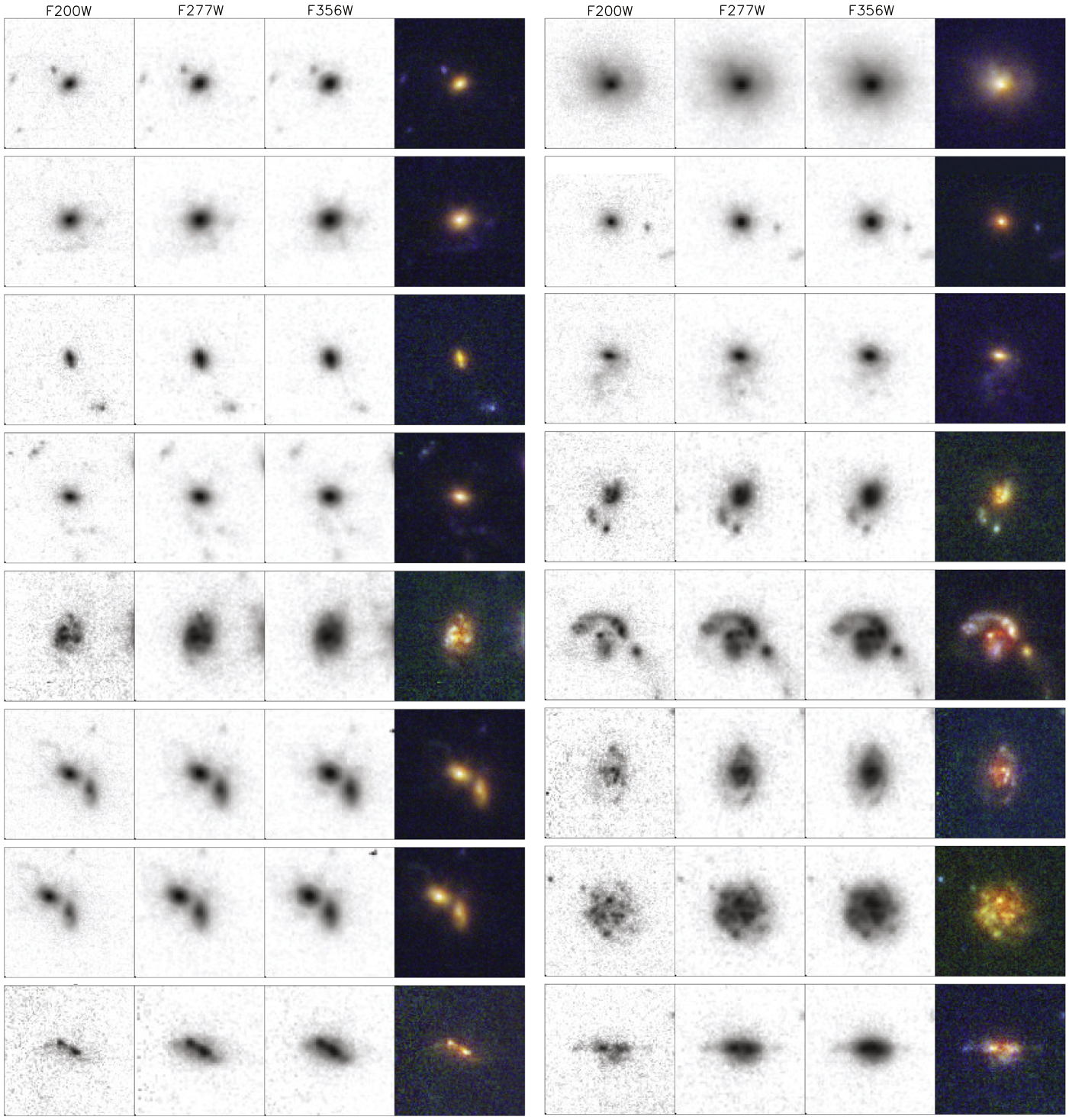

Figure 5. Multiwavelength image cutouts of our control sample of X-ray-undetected sources at $z > 3$. The RGB images are composed of images in the F150W, F200W, and F277W filters. All images are $3'' \times 3''$ in size.

5.1.2. Surface Brightness Profile Fitting

The results of our two-dimensional surface brightness profile fitting can be seen in Figure 7. The only source not fit with a Sérsic profile is AEGIS 482, which we find is best fit using a point-source model. In Figure 8, we show the residual images of these fits in five NIRCam bands ranging from F150W to F444W. While pointlike emission dominates the light from this source, we see extended structure that is visible in multiple bands. The underlying host appears particularly elongated at F200W. We also note a possible nearby companion or stellar clump (e.g., Förster Schreiber et al. 2011) in the residual images. The companion is most clearly discernible in F200W but is present in all five bands.

The hosts of AEGIS 495 and 511 are fit with Sérsic indices (n) of $n = 4.28 \pm 0.03$ and 3.49 ± 0.01, respectively, in agreement with our visual classification of these galaxies as spheroids. However, since the SED of AEGIS 511 was fit with a moderate AGN contribution, we also modeled it using a

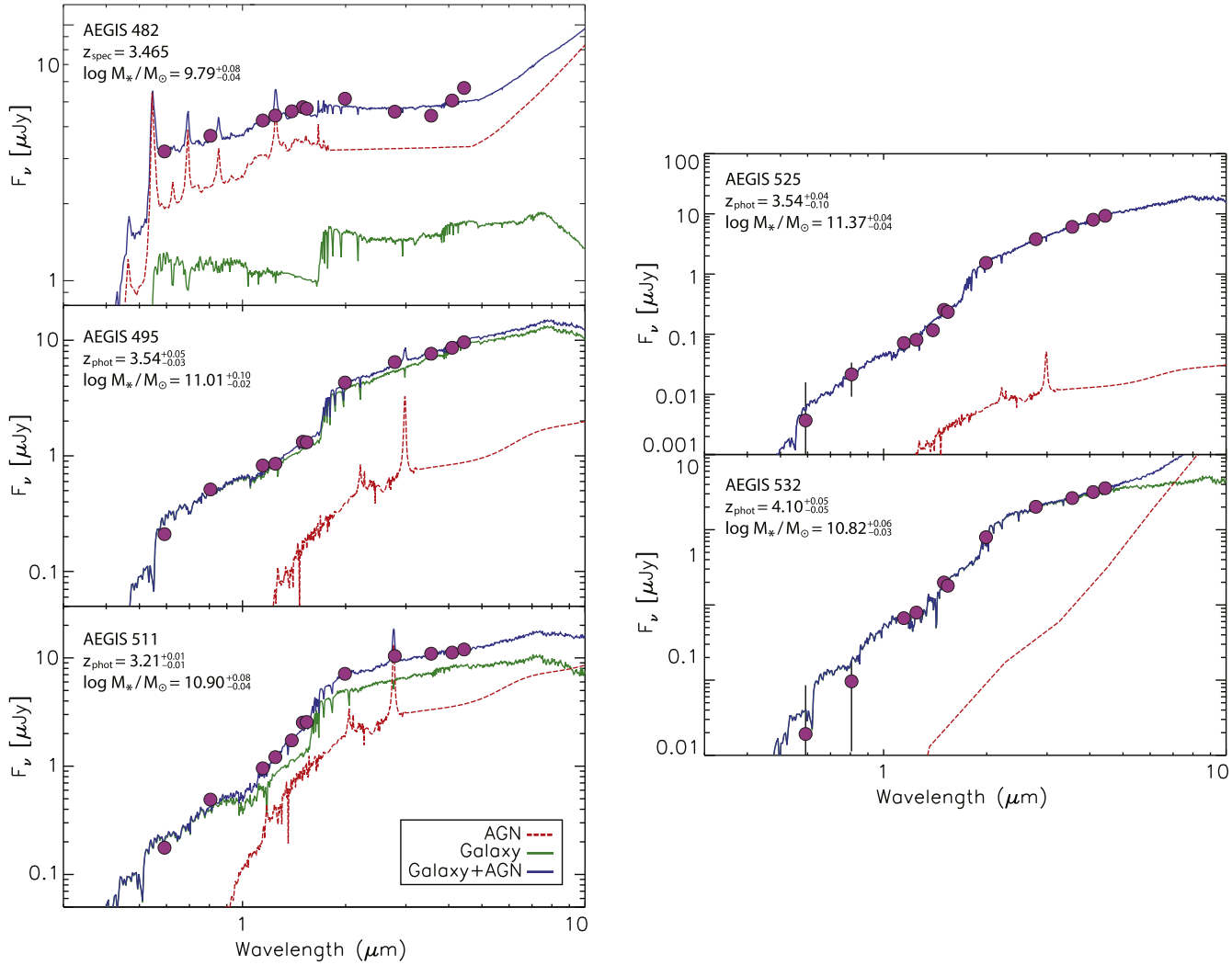

Figure 6. The SED fits for our five AGN hosts at $z > 3$. Our measured photometric data from JWST NIRCam and HST WFC3 and ACS are shown in magenta. The best-fit linear combination of each AGN template with each galaxy template in the full stellar population grid is shown in blue. The galaxy and AGN contributions are shown separately in green and red, respectively.

point-source component in addition to a Sérsic profile. The resulting fit attributes 17.6% of the light in F356W to the unresolved nuclear component, which reduces the resulting Sérsic index to $n = 2.24 \pm 0.02$.

A single Sérsic fit of AEGIS 525 results in $n = 4.20 \pm 0.04$, indicative of the prominent bulge in this system. We also performed a double Sérsic fit with one component fixed to an $n = 4$ de Vaucouleurs profile (de Vaucouleurs 1948). In this case, the second component is fit with a large effective radius ($r_e = 0\farcs43 \pm 0\farcs01$) and a relatively flat surface brightness profile ($n = 0.21 \pm 0.01$). The resulting bulge-to-total ratio of the galaxy is 0.69, consistent with a bulge-dominated disk.

The host of AEGIS 532, the most compact galaxy in the sample, is best fit with a small effective radius of $r_e = 0\farcs06 \pm 0\farcs01$ and a Sérsic index of $n = 1.14 \pm 0.05$. This raises the possibility that it is a massive compact disk such as those reported at $z \sim 2$ (e.g., van der Wel et al. 2011; Weinzirl et al. 2011). However, we caution that this fit may be impacted by the large nearby galaxy whose spiral structure is poorly fit with a single Sérsic profile.

Similar surface brightness profile fitting was carried out on each of our inactive control galaxies. We find that this sample has a lower average[58] Sérsic index compared to the AGN hosts, with $\bar{n}_{\rm control} = 1.6$ versus $\bar{n}_{\rm AGN} = 2.6$. Here we use the results of our single Sérsic fits in all cases except AEGIS 511, where we include an additional point-source component. This is in agreement with the results of our visual classifications, which found the control sample to have a larger fraction of disk-dominated systems. However, we do not find a significant difference in the effective radii of the two samples, with $\bar{r}_{\rm e,control} = 1.1$ kpc versus $\bar{r}_{\rm e,AGN} = 0.9$ kpc, reflecting the fact that many of the disks in the control sample are compact.

5.1.3. Nonparametric Morphologies

In Figure 9, we show the nonparametric morphology indicators of Gini versus M_{20} and concentration versus asymmetry for both the AGN sample and the inactive control sample. For this analysis, we have excluded AEGIS 482 and

[58] Here we use the geometric mean, which is a better indicator of the average value than the median or arithmetic mean when samples sizes are small.

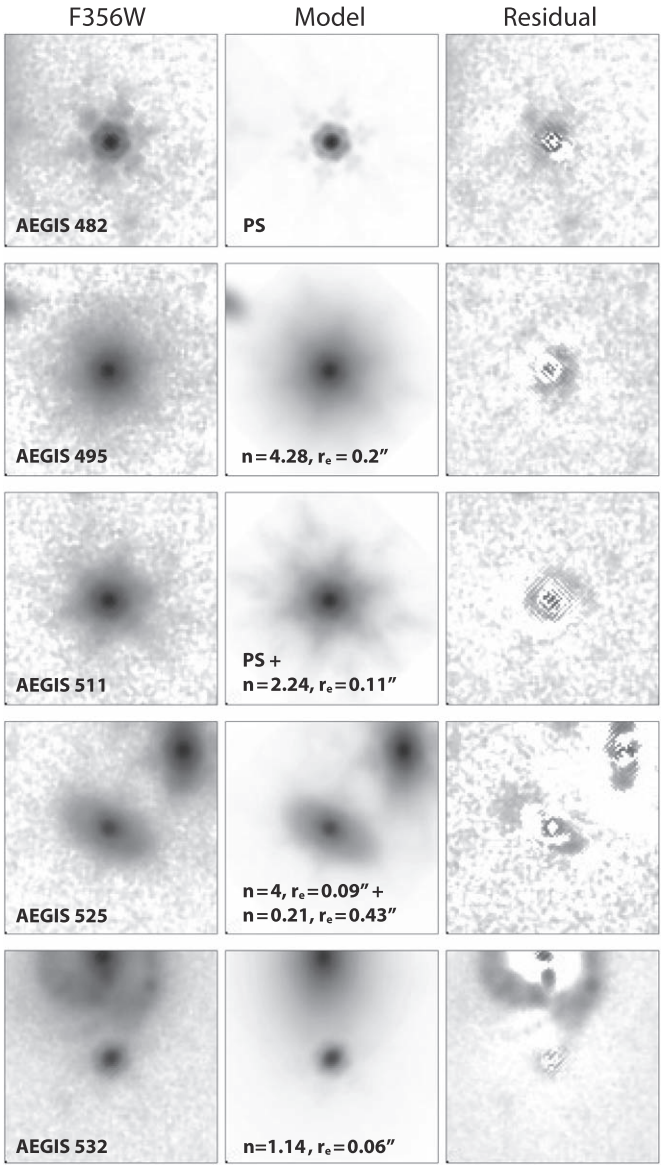

Figure 7. Results of our two-dimensional surface brightness profile fitting. The F356W images are shown in the left column, our best-fit GALFIT models are shown in the middle column, and the residuals (data minus model) are shown in the right column. The best-fit Sérsic index and effective radius for each source are listed. Here PS stands for "point source." Images are $3'' \times 3''$ in size.

run Statmorph on AEGIS 511 without making any corrections for nuclear light from the AGN. Points from both samples are color-coded based on their best-fit Sérsic index, and the background contours show the distribution of visually classified galaxies with disk, spheroid, and irregular morphologies in the five CANDELS fields at $1 < z < 3$ from Kartaltepe et al. (2015).

We find that the AGN sample is skewed toward higher Gini and lower M_{20} values clustering toward the bulge-dominated region of the diagram as defined by Lotz et al. (2004). This is evident when comparing the average value of the Gini–M_{20} bulge statistic, $F(G, M_{20})$. This statistic is a measure of position along the direction perpendicular to the line that divides early- and late-type galaxies, with its origin located where the two dashed lines in the left panel of Figure 9 intersect. The quantity is strongly correlated with bulge strength, with values increasing toward bulge-dominated systems. The AGN sample has an average Gini–M_{20} bulge statistic value of $\bar{F}(G, M_{20})_{\rm AGN} = 0.05$ compared to $\bar{F}(G, M_{20})_{\rm control} = -0.31$ for the control sample. This indicates that the AGN hosts are generally more bulge-dominated relative to their inactive counterparts, which is consistent with both our visual assessment and Sérsic profile fits.

In the concentration–asymmetry plane, we find that the AGN skew toward higher concentration values, with $\bar{C}_{\rm AGN} = 3.2$ and $\bar{C}_{\rm control} = 2.7$. Unlike our visual classifications, which found more disturbed morphologies among the control galaxies, we do not find a substantial difference between the average asymmetry values of the AGN and control samples. While many of the inactive galaxies with low Sérsic indices have higher asymmetry values relative to the AGN, a roughly equal number also scatter to lower asymmetry values, largely negating any difference.

5.2. Star Formation Activity

In Figure 10, we show the rest-frame $V - J$ versus $U - V$ colors of the five AGN hosts, both with and without correcting for AGN emission. The colors are determined by convolving the redshifted U, V, and J filter bandpasses with the best-fitting templates returned by FAST for each source. The open red circles show the color of the AGN+galaxy emission, while filled red circles denote galaxy-only emission corrected for any AGN contamination. The dashed green line denotes the color cut of Williams et al. (2009) for identifying quiescent galaxies, which Schreiber et al. (2018) showed continues to have high purity at $z = 3$–4 (although see Antwi-Danso et al. 2022 for an alternative color selection).

We find that AEGIS 511, AEGIS 525, and AEGIS 532 are all located within the quiescent boundary. AEGIS 525 lies near the red border of the quiescent region and is offset from the locus of quiescent galaxies observed at $z \sim 2$, which likely reflects additional dust reddening in this galaxy. Our SED modeling returns a best-fit dust attenuation (A_V) of 1.9 for this source, consistent with its redder UVJ color. AEGIS 495 sits just blueward of the lower $U - V$ boundary. This region is notable in that the bluer $U - V$ colors are consistent with young quiescent galaxies, such as those that have recently experienced a burst of star formation followed by a rapid truncation of activity (e.g., Whitaker et al. 2012; Schreiber et al. 2018). It suggests that this galaxy may be recently quenched or in a poststarburst phase. Finally, the best-fit galaxy template for AEGIS 482 places it squarely within the locus of unobscured star-forming galaxies.

To further assess the star formation activity of our sample, we compared their SFRs to that of the star-forming main sequence (e.g., Noeske et al. 2007) at $3 < z < 5$. The SFRs we measure for each AGN host based on our SED fitting can be found in Table 1. In Figure 11, we plot these SFRs versus host stellar mass, along with the SFRs of the general galaxy population at this redshift as measured by the CANDELS survey. The blue line denotes the star-forming main sequence as fit by Barro et al. (2019), and the red line denotes the redshift-dependent threshold used to select quiescent galaxies by Aird et al. (2018). We find that AEGIS 511, AEGIS 525, and AEGIS 532 are all below this threshold, while AEGIS 495 lies just above the quiescent limit. We reach a similar conclusion when considering the specific SFR (sSFR; the SFR per unit stellar mass) of our sample. The star-forming

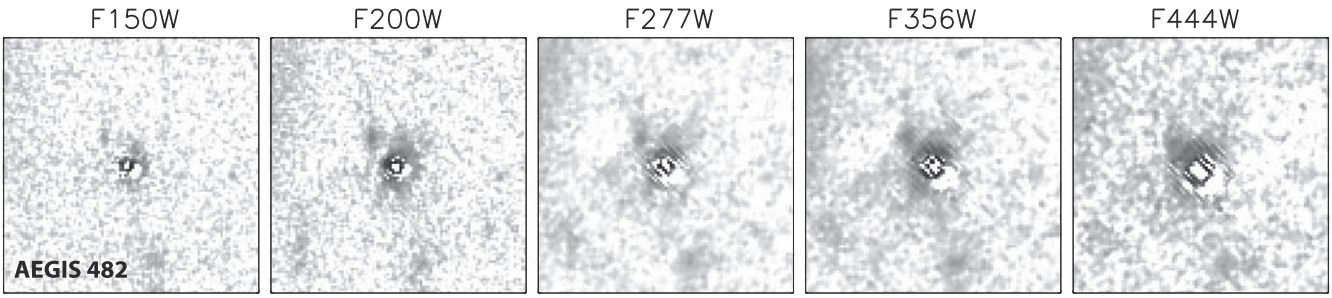

Figure 8. Residual images of AEGIS 482 after subtracting the best-fit point-source model in five NIRCam bands. Images are $3'' \times 3''$ in size.

main sequence at this redshift has an $\mathrm{sSFR_{MS}} = 1.5\ \mathrm{Gyr}^{-1}$ (Schreiber et al. 2017, 2018). We find that the hosts of AEGIS 511, AEGIS 525, and AEGIS 532 all have sSFRs that are a factor of 10 or more below that of the main sequence, while AEGIS 495 is suppressed by a smaller factor of 2.9, in general agreement with their *UVJ* colors.

Recently, Carnall et al. (2022) reported that the hosts of both AEGIS 525 and AEGIS 532 are quiescent. That study used the time-dependent quiescent selection criteria $\mathrm{sSFR} < 0.2/t_{\mathrm{obs}}$, where t_{obs} is the age of the universe at the redshift of the galaxy. We find that AEGIS 511, AEGIS 525, and AEGIS 532 would all be considered quiescent using this criterion, while AEGIS 495 lies just above the threshold. Coupled with its location in the poststarburst region of the *UVJ* diagram, this suggests that the host of AEGIS 495 is the sole well-resolved galaxy in our sample with a moderate level of ongoing star formation, albeit potentially suppressed relative to that of the star-forming main sequence.

As a final check, we investigated whether any of these sources might be dusty starburst galaxies masquerading as quiescent systems by examining their far-infrared emission using data from Herschel PACS (100 and 160 μm; Lutz et al. 2011) and SPIRE (250, 350, and 500 μm; Oliver et al. 2012). We make use of prior-fitted multiband photometry from A. Le Bail et al. (2022, in preparation), who employed the "super-deblended" technique of Liu et al. (2018) and Jin et al. (2018). None of the sources in our sample are directly detected, and the 2σ upper limits on their SFRs range from 110 to 150 $M_{\odot}\ \mathrm{yr}^{-1}$ for all five galaxies, consistent with our SED fits.

We also examined the star formation activity of our inactive control sample. In Figures 10 and 11, we show the the *UVJ* colors and SFRs, respectively, of these galaxies alongside the AGN hosts. We find that these galaxies consist of roughly an equal number of star-forming and quiescent systems. We see a bimodal *UVJ* color distribution, with nine galaxies in the quiescent and poststarburst regions of the *UVJ* diagram and seven galaxies with colors consistent with dusty star-forming systems. In the SFR–mass plane, we find the control galaxies distributed equally around the Aird et al. (2018) quiescent threshold, with eight galaxies above and eight below this limit. Given the small size of both the control and AGN samples, the fractions of both populations that are quiescent are statistically consistent with each other: $50\% \pm 12\%$ (8/16) for the control and $60\%^{+16\%}_{-22\%}$ (3/5) for the AGN.

6. Discussion

We examine the rest-frame optical host properties of five X-ray-luminous AGN detected at $3 < z < 5$ using JWST NIRCam imaging taken as part of the CEERS program. Four of the hosts are spatially well resolved, and a visual assessment of their morphologies reveals that three are spheroidal systems and one is a bulge-dominated disk. None of the galaxies show strong morphological disturbances indicative of a recent interaction or merger event; however, point-source subtraction reveals a potential close companion near the most X-ray-luminous AGN in the sample. Compared to an inactive control sample of galaxies with similar mass and redshift, we find the AGN hosts to be more bulge-dominated based on our parametric and nonparametric morphology indicators and less disturbed based on our visual classifications. We find that the four resolved hosts have rest-frame colors that place them in the quiescent and poststarburst regions of the *UVJ* diagram. We also perform two-component SED fits using both galaxy and AGN templates and find that the sSFRs of all four galaxies are at least a factor of $\sim$3 below the star-forming main sequence at $z = 3.5$, confirming that they have recently quenched or are potentially in the process of quenching.

The small sample size notwithstanding, the properties of these galaxies stand in contrast to those measured among the bulk of the AGN population at $z \sim 2$, where hosts are predominately normal star-forming systems with a large disk fraction (e.g., Schawinski et al. 2011; Kocevski et al. 2012; Mullaney et al. 2012; Rosario et al. 2013; Florez et al. 2020; Ji et al. 2022). However, AGN activity is not uncommon among the quiescent population at these redshifts. Studies find that 20%–25% of massive ($M_* > 10^{10}\ M_{\odot}$) quiescent galaxies host an X-ray AGN at $z \sim 2$ (Kocevski et al. 2017; Wang et al. 2017), a fivefold increase over the fraction measured at $z \sim 1$ (e.g., Georgakakis et al. 2008). This fraction increases further at higher redshifts, where Schreiber et al. (2018) reported that 33% of their sample of young massive quiescent galaxies at $3 < z < 4$ are X-ray-detected. Furthermore, Forrest et al. (2020a) noted that 44% of their sample of massive ($M_* > 10^{11}\ M_{\odot}$) quiescent galaxies at this same redshift are likely AGN based on their emission line ratios. This strong evolution in AGN fraction implies a much higher AGN duty cycle in passive galaxies at these redshifts. In fact, Aird et al. (2018) reported that the AGN duty cycle among quiescent galaxies at $z > 2$ is equivalent to that of star-forming galaxies of similar mass and redshift. Coupled with the host properties that we observe in our sample, this suggests that distant quiescent galaxies have increased residual cold-gas reservoirs that can continue to fuel SMBH growth even after star formation has been curtailed.

This is not to say that the AGN population is dominated by quiescent galaxies at this redshift, as previous studies with HST have found that the black hole accretion rate and host SFR are

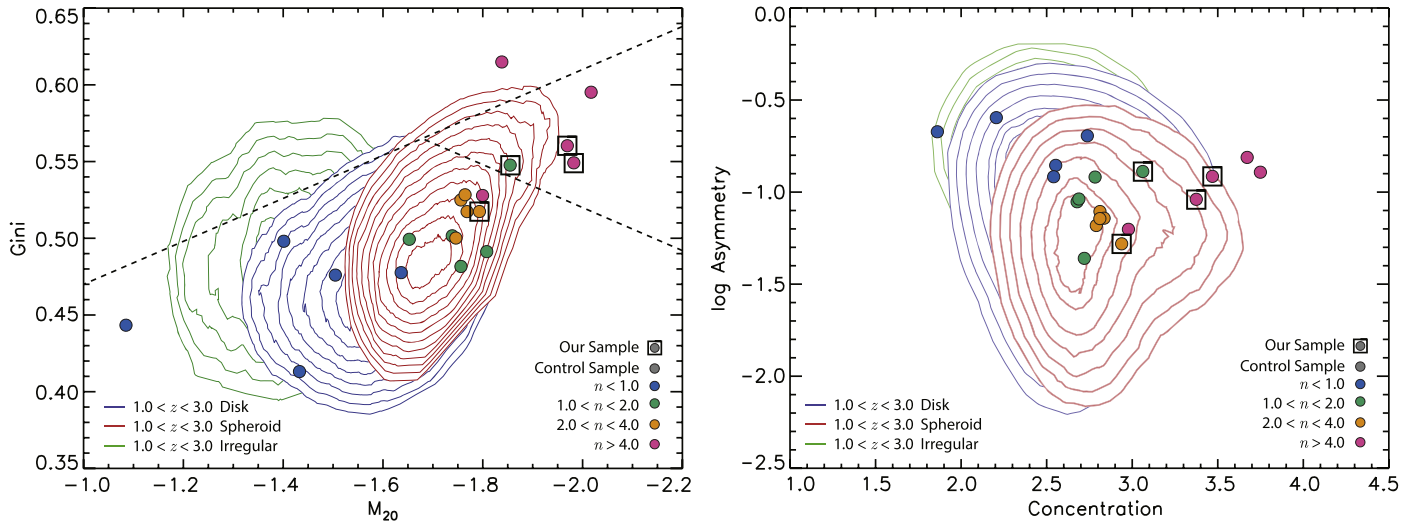

Figure 9. Nonparametric morphology indicators for our $z > 3$ AGN and control samples. Left: Gini value vs. M_{20}, with dashed lines representing the merger (top left), disk-dominated (bottom left), and bulge-dominated (top right) regions defined in Lotz et al. (2004). Right: asymmetry vs. concentration. Each galaxy is color-coded based on its best-fit Sérsic index. The background contours are all visually classified galaxies in the five CANDELS fields at $1 < z < 3$ from Kartaltepe et al. (2015), color-coded based on their morphology.

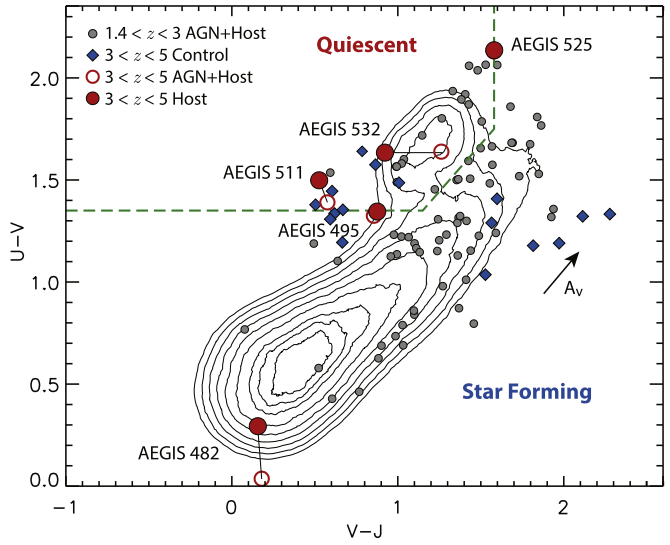

Figure 10. The *UVJ* color diagram. Open red circles show the rest-frame colors of the AGN+galaxy emission of our $3 < z < 5$ sample, while filled red circles are colors corrected for the AGN emission predicted in each band from our two-component SED fits. Blue diamonds denote our inactive control sample. Contours and gray circles show the color distribution of galaxies and the hosts of X-ray-selected AGN, respectively, in the redshift range $1.4 < z < 3.0$ in the CANDELS fields. The green dashed line denotes the dividing line used to separate quiescent and star-forming galaxies.

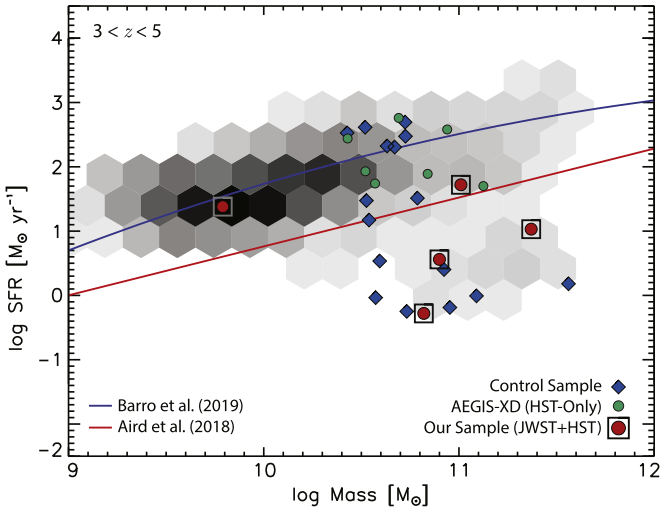

Figure 11. The SFR vs. stellar mass for AGN hosts in the EGS field at $3 < z < 5$. The five X-ray AGN observed by CEERS at this redshift are shown as boxed red circles. AEGIS-XD sources that fall outside of the current CEERS footprint but were observed by the CANDELS survey are shown as green circles. Blue diamonds denote our inactive control sample. The background hexagonal bins show the relative number of galaxies in this redshift range over all five of the CANDELS fields. The curved blue line is the best-fit star-forming main sequence reported in Barro et al. (2019), while the red line is the threshold used for selecting quiescent galaxies in Aird et al. (2018).

correlated out to at least $z \sim 4$–5 (Aird et al. 2018; Suh et al. 2019). In Figure 11, we show the X-ray AGN in EGS that were observed by the CANDELS survey but currently fall outside of the CEERS imaging. These galaxies are all located in the star-forming region of the diagram, suggesting that the AGN host population could distribute equally around the quiescent cut when we expand our sample.

However, the ubiquity of AGN in massive quiescent galaxies at $z > 3$ is notable because energy injection from AGN has been widely used in semianalytic models and cosmological simulations as a key quenching mechanism. The need for strong feedback is particularly acute for massive quiescent galaxies at the redshifts of our sample given the limited time available (1–2 Gyr) to form them and fully shut down their star formation activity.

If these host galaxies were rapidly quenched as described by the radiative (or quasar) mode feedback model, where AGN-driven winds help to remove a galaxy's cold-gas supply, then we would be observing them in the postblowout phase, when the obscuring column density has dropped enough for the AGN to be visible, and the star formation and nuclear activity are in gradual decline. A galaxy in a similar state was recently reported by Kubo et al. (2022), who detected a type 2 QSO in a massive ($M_* = 10^{11.3}\ M_\odot$) quiescent galaxy at $z = 3.09$. In that case, strong ionized gas outflows are detected via broad [O III] emission, providing direct evidence of energy injection by the

AGN. Follow-up observations will be needed to confirm if similar outflows are present in our sample, but this example demonstrates a plausible scenario to explain the host properties that we observe.

Of course, one proposed mechanism for triggering quasar mode feedback is major galaxy–galaxy mergers, which are thought to prompt the radiatively efficient accretion that ultimately powers the quenching outflows. With the exception of AEGIS 482, which shows signs of a possible companion in the GALFIT residual images, our hosts do not exhibit the strong morphological disturbances that might be expected if these systems experienced a recent major merger event. A delay between the merger and the onset of AGN activity that is longer than the relaxation time of a galaxy (typically a few hundred megayears; Lotz et al. 2010), coupled with surface brightness dimming, might cause the most obvious merger signatures to fade below our detection limit. Such time lags are expected (Springel et al. 2005b; Di Matteo et al. 2005) and often invoked as a possible explanation for the lack of merger signatures in AGN hosts (e.g., Cisternas et al. 2011; Kocevski et al. 2012). However, AEGIS 525, which has a significant disk component, is unlikely to have experienced a major disruptive merger in the recent past. Although disks can reform following a gas-rich merger (Robertson et al. 2006; Bundy et al. 2010), the timescale required ($\sim$1 Gyr) makes this unlikely given the redshift of the source.

It should be noted that for moderate-luminosity AGN, like many in our sample, the implied black hole mass accretion rate is modest (a few $M_{\odot}$ yr^{-1} for $L_{\rm bol}/L_{\rm X} \sim 30$ and a radiative efficiency of 0.1) and could be sustained over several duty cycles with only modest amounts of gas ($\sim 10^9\,M_{\odot}$). If such gas reservoirs, which are common in the circumnuclear region of local spiral galaxies, are present in the circumnuclear region of $z > 3$ galaxies, they can readily fuel such AGN without the need for large-scale gas transport by mergers, as long as local circumnuclear processes can drain angular momentum from the gas and drive it down to the black hole accretion disk (e.g., Jogee 2006; Hopkins et al. 2014). Recent studies have found an upper limit on the cold-gas fraction of massive ($M_* \sim 10^{11}\,M_{\odot}$) quiescent galaxies at $z = 3.5$ of 20% (Suzuki et al. 2022), which would allow for gas reservoirs of order $\sim 10^9\,M_{\odot}$ in our AGN hosts.

Alternative triggering mechanisms include minor mergers or rapid cold flow accretion (Dekel et al. 2009), which can funnel gas to the centers of galaxies on short timescales (Bournaud et al. 2011, 2012). According to recent studies using cosmological hydrodynamic simulations, these mechanisms may in fact be responsible for triggering the bulk of AGN activity at early times rather than major mergers (Steinborn et al. 2018; Sharma et al. 2021).

Whether the initial quenching of these galaxies is ultimately due to AGN feedback or another cause, such as simple rapid gas exhaustion, remains to be determined. However, the presence of luminous AGN in these systems and the observed high duty cycle in massive quiescent galaxies at similar redshifts implies that AGN can input a significant amount of energy into their hosts after star formation has ceased, which may heat the halos of these systems and prevent renewed star formation. A larger sample size will be needed to determine if this is a common role that moderate-luminosity AGN play during the era of galaxy assembly.

7. Conclusions

We report on the host properties of five X-ray-luminous AGN identified at $3 < z < 5$ in the first epoch of NIRCam imaging from the CEERS ERS program. We examine their host morphologies using a combination of visual classification, nonparametric morphology indicators, and surface brightness profile fitting. We also examine their star formation activity using rest-frame colors and SFRs derived through SED modeling, where we employ both galaxy and AGN templates. The properties of the AGN hosts are compared against a control sample of inactive galaxies (i.e., those with no X-ray detection) matched in mass and redshift. We find the following.

1. Three of the AGN hosts (AEGIS 495, 511, and 532) have spheroidal morphologies, one (AEGIS 525) is a bulge-dominated disk, and one (AEGIS 482) is dominated by pointlike emission. Our point-source subtraction reveals the underlying host of AEGIS 482 to be elongated, with a possible nearby companion. Otherwise, none of the hosts show strong morphological disturbances that might indicate a recent interaction or merger event.
2. Compared to the inactive control sample, the AGN hosts are more bulge-dominated, having a higher average Sérsic index (2.6 versus 1.6) and Gini–M_{20} bulge statistic (0.05 versus -0.31). The AGN are also less disturbed than the control sample, 50% of which show some level of asymmetry or distortion in their morphology.
3. The colors of three AGN hosts place them within the quiescent region of the *UVJ* diagram, including AEGIS 525, which appears to be a passive disk. One host (AEGIS 495) has a bluer $U - V$ color that is consistent with a poststarburst stellar population. The best-fit galaxy template for AEGIS 482, the point source–dominated host, has colors that place it squarely in the locus of star-forming galaxies.
4. The SFRs of the AGN hosts, measured from our two-component SED fitting, agree well with the star formation activity inferred from their *UVJ* colors. The three hosts in the quiescent region of the *UVJ* diagram have sSFRs that are an order of magnitude or more below that of the star-forming main sequence at $z \sim 3.5$, while AEGIS 495, the poststarburst host, is suppressed by a smaller factor of 2.9.

An elevated AGN fraction among quiescent galaxies at $z > 3$ suggests that these galaxies have an increased residual cold-gas supply relative to their lower-redshift counterparts. Given the age of the universe at these redshifts, our quiescent hosts must all be observed soon after the shutdown of their star formation activity. Whether the AGN plays a role in this suppression (either by initially quenching them or by helping to maintain their quiescence state by continuing to inject energy into the systems after quenching) remains to be determined. In future papers, we plan to expand our sample size using the full CEERS data set, which will include both additional NIRCam imaging and spectroscopic observations of AGN hosts during the epoch of galaxy assembly.

We thank the anonymous reviewer for the helpful comments and suggestions. This work is supported by NASA grants JWST-ERS-01345 and JWST-AR-02446 and based on observations made with the NASA/ESA/CSA James Webb Space Telescope. The data were obtained from the Mikulski Archive

for Space Telescopes at the Space Telescope Science Institute, which is operated by the Association of Universities for Research in Astronomy, Inc., under NASA contract NAS 5–03127 for JWST. This work also made use of the Rainbow Cosmological Surveys Database, which is operated by the Centro de Astrobiología (CAB/INTA), partnered with the University of California Observatories at Santa Cruz (UCO/Lick, UCSC).

ORCID iDs

Dale D. Kocevski https://orcid.org/0000-0002-8360-3880
Guillermo Barro https://orcid.org/0000-0002-0786-7307
Elizabeth J. McGrath https://orcid.org/0000-0001-8688-2443
Steven L. Finkelstein https://orcid.org/0000-0001-8519-1130
Micaela B. Bagley https://orcid.org/0000-0002-9921-9218
Henry C. Ferguson https://orcid.org/0000-0001-7113-2738
Shardha Jogee https://orcid.org/0000-0002-1590-0568
Guang Yang https://orcid.org/0000-0001-8835-7722
Mark Dickinson https://orcid.org/0000-0001-5414-5131
Nimish P. Hathi https://orcid.org/0000-0001-6145-5090
Bren E. Backhaus https://orcid.org/0000-0001-8534-7502
Eric F. Bell https://orcid.org/0000-0002-5564-9873
Laura Bisigello https://orcid.org/0000-0003-0492-4924
Véronique Buat https://orcid.org/0000-0003-3441-903X
Denis Burgarella https://orcid.org/0000-0002-4193-2539
Caitlin M. Casey https://orcid.org/0000-0002-0930-6466
Nikko J. Cleri https://orcid.org/0000-0001-7151-009X
M. C. Cooper https://orcid.org/0000-0003-1371-6019
Luca Costantin https://orcid.org/0000-0001-6820-0015
Darren Croton https://orcid.org/0000-0002-5009-512X
Emanuele Daddi https://orcid.org/0000-0002-3331-9590
Adriano Fontana https://orcid.org/0000-0003-3820-2823
Seiji Fujimoto https://orcid.org/0000-0001-7201-5066
Jonathan P. Gardner https://orcid.org/0000-0003-2098-9568
Eric Gawiser https://orcid.org/0000-0003-1530-8713
Mauro Giavalisco https://orcid.org/0000-0002-7831-8751
Andrea Grazian https://orcid.org/0000-0002-5688-0663
Norman A. Grogin https://orcid.org/0000-0001-9440-8872
Yuchen Guo https://orcid.org/0000-0002-4162-6523
Pablo Arrabal Haro https://orcid.org/0000-0002-7959-8783
Michaela Hirschmann https://orcid.org/0000-0002-3301-3321
Benne W. Holwerda https://orcid.org/0000-0002-4884-6756
Marc Huertas-Company https://orcid.org/0000-0002-1416-8483
Taylor A. Hutchison https://orcid.org/0000-0001-6251-4988
Kartheik G. Iyer https://orcid.org/0000-0001-9298-3523
Stéphanie Juneau https://orcid.org/0000-0002-0000-2394
Jeyhan S. Kartaltepe https://orcid.org/0000-0001-9187-3605
Lisa J. Kewley https://orcid.org/0000-0001-8152-3943
Allison Kirkpatrick https://orcid.org/0000-0002-1306-1545
Anton M. Koekemoer https://orcid.org/0000-0002-6610-2048
Peter Kurczynski https://orcid.org/0000-0002-8816-5146
Aurélien Le Bail https://orcid.org/0000-0002-9466-2763
Arianna S. Long https://orcid.org/0000-0002-7530-8857
Jennifer M. Lotz https://orcid.org/0000-0003-3130-5643
Ray A. Lucas https://orcid.org/0000-0003-1581-7825
Casey Papovich https://orcid.org/0000-0001-7503-8482
Laura Pentericci https://orcid.org/0000-0001-8940-6768
Pablo G. Pérez-González https://orcid.org/0000-0003-4528-5639
Nor Pirzkal https://orcid.org/0000-0003-3382-5941
Marc Rafelski https://orcid.org/0000-0002-9946-4731
Swara Ravindranath https://orcid.org/0000-0002-5269-6527
Rachel S. Somerville https://orcid.org/0000-0002-6748-6821
Amber N. Straughn https://orcid.org/0000-0002-4772-7878
Sandro Tacchella https://orcid.org/0000-0002-8224-4505
Jonathan R. Trump https://orcid.org/0000-0002-1410-0470
Stephen M. Wilkins https://orcid.org/0000-0003-3903-6935
Stijn Wuyts https://orcid.org/0000-0003-3735-1931
L. Y. Aaron Yung https://orcid.org/0000-0003-3466-035X
Jorge A. Zavala https://orcid.org/0000-0002-7051-1100

References

Abraham, R. G., van den Bergh, S., & Nair, P. 2003, ApJ, 588, 218
Aird, J., Coil, A. L., & Georgakakis, A. 2018, MNRAS, 474, 1225
Antwi-Danso, J., Papovich, C., Leja, J., et al. 2022, arXiv:2207.07170
Barro, G., Perez-Gonzalez, P. G., Cava, A., et al. 2019, ApJS, 243, 22
Barro, G., Pérez-González, P. G., Gallego, J., et al. 2011a, ApJS, 193, 13
Barro, G., Pérez-González, P. G., Gallego, J., et al. 2011b, ApJS, 193, 30
Benson, A. J., Bower, R. G., Frenk, C. S., et al. 2003, ApJ, 599, 38
Bershady, M. A., Jangren, A., & Conselice, C. J. 2000, AJ, 119, 2645
Bertin, E., & Arnouts, S. 1996, A&AS, 117, 393
Bournaud, F., Chapon, D., Teyssier, R., et al. 2011, ApJ, 730, 4
Bournaud, F., Juneau, S., Le Floc'h, E., et al. 2012, ApJ, 757, 81
Bower, R. G., Benson, A. J., Malbon, R., et al. 2006, MNRAS, 370, 645
Brammer, G. B., van Dokkum, P. G., & Coppi, P. 2008, ApJ, 686, 1503
Brammer, G. B., van Dokkum, P. G., Franx, M., et al. 2012, ApJS, 200, 13
Bruzual, G., & Charlot, S. 2003, MNRAS, 344, 1000
Bundy, K., Scarlata, C., Carollo, C. M., et al. 2010, ApJ, 719, 1969
Carnall, A. C., McLeod, D. J., McLure, R. J., et al. 2022, arXiv:2208.00986
Casertano, S., de Mello, D., Dickinson, M., et al. 2000, AJ, 120, 2747
Chabrier, G. 2003, PASP, 115, 763
Chen, Z., Faber, S. M., Koo, D. C., et al. 2020, ApJ, 897, 102
Choi, E., Ostriker, J. P., Naab, T., Oser, L., & Moster, B. P. 2015, MNRAS, 449, 4105
Cisternas, M., Jahnke, K., Inskip, K. J., et al. 2011, ApJ, 726, 57
Conroy, C., & Gunn, J. E. 2010, FSPS: Flexible Stellar Population Synthesis, Astrophysics Source Code Library, ascl:1010.043
Conroy, C., Gunn, J. E., & White, M. 2009, ApJ, 699, 486
Conselice, C. J. 2003, ApJS, 147, 1
Conselice, C. J., Bershady, M. A., & Jangren, A. 2000, ApJ, 529, 886
Croton, D. J., Springel, V., White, S. D. M., et al. 2006, MNRAS, 365, 11
Dave, R., Angles-Alcazar, D., Narayanan, D., et al. 2019, MNRAS, 486, 2827
de Vaucouleurs, G. 1948, AnAp, 11, 247
Dekel, A., Sari, R., & Ceverino, D. 2009, ApJ, 703, 785
Di Matteo, T., Springel, V., & Hernquist, L. 2005, Natur, 433, 604
Ding, X., Silverman, J. D., & Onoue, M. 2022, arXiv:2209.03359
Donley, J. L., Kartaltepe, J., Kocevski, D., et al. 2018, ApJ, 853, 63
Dubois, Y., Peirani, S., Pichon, C., et al. 2016, MNRAS, 463, 3948
Ebeling, H., White, D. A., & Rangarajan, F. V. N. 2006, MNRAS, 368, 65
Ferrarese, L., & Merritt, D. 2000, ApJL, 539, L9
Finkelstein, S. L., Bagley, M. B., Arrabal Haro, P., et al. 2022, arXiv:2207.12474
Florez, J., Jogee, S., Guo, Y., et al. 2021, MNRAS, 508, 762
Florez, J., Jogee, S., Sherman, S., et al. 2020, MNRAS, 497, 3273
Forrest, B., Annunziatella, M., Wilson, G., et al. 2020b, ApJL, 890, L1
Forrest, B., Marsan, Z. C., Annunziatella, M., et al. 2020a, ApJ, 903, 47
Förster Schreiber, N. M., Shapley, A. E., Genzel, R., et al. 2011, ApJ, 739, 45
Fruchter, A. S., & Hook, R. N. 2002, PASP, 114, 144
Gardner, J. P., Mather, J. C., Clampin, M., et al. 2006, SSRv, 123, 485
Gebhardt, K., Bender, R., Bower, G., et al. 2000, ApJL, 539, L13
Georgakakis, A., Nandra, K., Yan, R., et al. 2008, MNRAS, 385, 2049
Grogin, N. A., Conselice, C. J., Chatzichristou, E., et al. 2005, ApJL, 627, L97
Grogin, N. A., Kocevski, D. D., Faber, S. M., et al. 2011, ApJS, 197, 35
Harrison, C. M., Alexander, D. M., Mullaney, J. R., et al. 2012, ApJL, 760, L15
Hirschmann, M., Somerville, R. S., Naab, T., & Burkert, A. 2012, MNRAS, 426, 237
Hopkins, P. F., Cox, T. J., Kereš, D., & Hernquist, L. 2008a, ApJS, 175, 390
Hopkins, P. F., Hernquist, L., Cox, T. J., et al. 2006, ApJS, 163, 1
Hopkins, P. F., Hernquist, L., Cox, T. J., & Kereš, D. 2008b, ApJS, 175, 356
Hopkins, P. F., Kocevski, D. D., & Bundy, K. 2014, MNRAS, 445, 823
Ji, Z., Giavalisco, M., Kirkpatrick, A., et al. 2022, ApJ, 925, 74
Jin, S., Daddi, E., Liu, D., et al. 2018, ApJ, 864, 56

Jogee, S. 2006, in Physics of Active Galactic Nuclei at all Scales, ed. D. Alloin, R. Johnson, & P. Lira (Berlin: Springer), 143
Kartaltepe, J. S., Mozena, M., Kocevski, D., et al. 2015, ApJS, 221, 11
Kauffmann, G., & Haehnelt, M. 2000, MNRAS, 311, 576
Kirkpatrick, A., Sharon, C., Keller, E., & Pope, A. 2019, ApJ, 879, 41
Kocevski, D. D., Barro, G., Faber, S. M., et al. 2017, ApJ, 846, 112
Kocevski, D. D., Brightman, M., Nandra, K., et al. 2015, ApJ, 814, 104
Kocevski, D. D., Faber, S. M., Mozena, M., et al. 2012, ApJ, 744, 148
Koekemoer, A. M., Faber, S. M., Ferguson, H. C., et al. 2011, ApJS, 197, 36
Koss, M., Mushotzky, R., Veilleux, S., & Winter, L. 2010, ApJL, 716, L125
Kriek, M., & Conroy, C. 2013, ApJL, 775, L16
Kriek, M., van Dokkum, P. G., Franx, M., Illingworth, G. D., & Magee, D. K. 2009, ApJL, 705, L71
Kubo, M., Umehata, H., Matsuda, Y., et al. 2022, arXiv:2207.03628
Labbe, I., van Dokkum, P., Nelson, E., et al. 2022, arXiv:2207.12446
Liu, D., Daddi, E., Dickinson, M., et al. 2018, ApJ, 853, 172
Lotz, J. M., Jonsson, P., Cox, T. J., & Primack, J. R. 2010, MNRAS, 404, 575
Lotz, J. M., Primack, J., & Madau, P. 2004, AJ, 128, 163
Lutz, D., Poglitsch, A., Altieri, B., et al. 2011, A&A, 532, A90
Magorrian, J., Tremaine, S., Richstone, D., et al. 1998, AJ, 115, 2285
Maraston, C., Pforr, J., Renzini, A., et al. 2010, MNRAS, 407, 830
McConnell, N. J., & Ma, C.-P. 2013, ApJ, 764, 184
Morishita, T., Abramson, L. E., Treu, T., et al. 2019, ApJ, 877, 141
Mountrichas, G., Buat, V., Yang, G., et al. 2021, A&A, 653, A74
Mountrichas, G., Buat, V., Yang, G., et al. 2022, A&A, 663, A130
Mullaney, J. R., Daddi, E., Bethermin, M., et al. 2012, ApJL, 753, L30
Nandra, K., Georgakakis, A., Willmer, C. N. A., et al. 2007, ApJL, 660, L11
Nandra, K., Laird, E. S., Aird, J. A., et al. 2015, ApJS, 220, 10
Newman, J. A., Cooper, M. C., Davis, M., et al. 2013, ApJS, 208, 5
Noeske, K. G., Weiner, B. J., Faber, S. M., et al. 2007, ApJL, 660, L43
Oliver, S. J., Bock, J., Altieri, B., et al. 2012, MNRAS, 424, 1614
Peng, C. Y., Ho, L. C., Impey, C. D., & Rix, H.-W. 2002, AJ, 124, 266
Pierce, C. M., Lotz, J. M., Laird, E. S., et al. 2007, ApJL, 660, L19
Polletta, M., Tajer, M., Maraschi, L., et al. 2007, ApJ, 663, 81
Robertson, B., Bullock, J. S., Cox, T. J., et al. 2006, ApJ, 645, 986
Rodriguez-Gomez, V., Snyder, G. F., Lotz, J. M., et al. 2019, MNRAS, 483, 4140
Rosario, D. J., McIntosh, D. H., van der Wel, A., et al. 2015, A&A, 573, A85
Rosario, D. J., Santini, P., Lutz, D., et al. 2013, ApJ, 771, 63
Sanders, D. B., Soifer, B. T., Elias, J. H., et al. 1988, ApJ, 325, 74
Satyapal, S., Ellison, S. L., McAlpine, W., et al. 2014, MNRAS, 441, 1297
Schawinski, K., Kaviraj, S., Khochfar, S., et al. 2007, ApJS, 173, 512
Schawinski, K., Treister, E., Urry, C. M., et al. 2011, ApJL, 727, L31
Schreiber, C., Glazebrook, K., Nanayakkara, T., et al. 2018, A&A, 618, A85
Schreiber, C., Pannella, M., Leiton, R., et al. 2017, A&A, 599, A134
Sérsic, J. L. 1968, Atlas de Galaxias Australes (Cordoba: Observatorio Astronomico)
Sharma, R. S., Choi, E., Somerville, R. S., et al. 2021, arXiv:2101.01729
Silva, L., Maiolino, R., & Granato, G. L. 2004, MNRAS, 355, 973
Snyder, G. F., Torrey, P., Lotz, J. M., et al. 2015, MNRAS, 454, 1886
Somerville, R. S., & Dave, R. 2015, ARA&A, 53, 51
Somerville, R. S., Hopkins, P. F., Cox, T. J., Robertson, B. E., & Hernquist, L. 2008, MNRAS, 391, 481
Springel, V., Di Matteo, T., & Hernquist, L. 2005a, ApJL, 620, L79
Springel, V., White, S. D. M., Jenkins, A., et al. 2005b, Natur, 435, 629
Stacey, H. R., McKean, J. P., Powell, D. M., et al. 2021, MNRAS, 500, 3667
Stanley, F., Harrison, C. M., Alexander, D. M., et al. 2015, MNRAS, 453, 591
Steinborn, L. K., Hirschmann, M., Dolag, K., et al. 2018, MNRAS, 481, 341
Suh, H., Civano, F., Hasinger, G., et al. 2019, ApJ, 872, 168
Sun, M., Trump, J. R., Brandt, W. N., et al. 2015, ApJ, 802, 14
Sutherland, W., & Saunders, W. 1992, MNRAS, 259, 413
Suzuki, T. L., Glazebrook, K., Schreiber, C., et al. 2022, ApJ, 936, 61
van der Wel, A., Rix, H.-W., Wuyts, S., et al. 2011, ApJ, 730, 38
Villforth, C., Hamann, F., Rosario, D. J., et al. 2014, MNRAS, 439, 3342
Wang, T., Elbaz, D., Alexander, D. M., et al. 2017, A&A, 601, A63
Ward, S. R., Harrison, C. M., Costa, T., & Mainieri, V. 2022, MNRAS, 514, 2936
Weinberger, R., Springel, V., Pakmor, R., et al. 2018, MNRAS, 479, 4056
Weinzirl, T., Jogee, S., Conselice, C. J., et al. 2011, ApJ, 743, 87
Whitaker, K. E., van Dokkum, P. G., Brammer, G., & Franx, M. 2012, ApJL, 754, L29
Williams, R. J., Quadri, R. F., Franx, M., van Dokkum, P., & Labbe, I. 2009, ApJ, 691, 1879
Yang, G., Boquien, M., Buat, V., et al. 2020, MNRAS, 491, 740
Yung, L. Y. A., Somerville, R. S., Finkelstein, S. L., et al. 2021, MNRAS, 508, 2706
Yung, L. Y. A., Somerville, R. S., Finkelstein, S. L., Popping, G., & Davé, R. 2019a, MNRAS, 483, 2983
Yung, L. Y. A., Somerville, R. S., Popping, G., et al. 2019b, MNRAS, 490, 2855